

<b>REPORT DOCUMENTATION PAGE</b>			Form Approved OMB NO. 0704-0188		
<p>The public reporting burden for this collection of information is estimated to average 1 hour per response, including the time for reviewing instructions, searching existing data sources, gathering and maintaining the data needed, and completing and reviewing the collection of information. Send comments regarding this burden estimate or any other aspect of this collection of information, including suggestions for reducing this burden, to Washington Headquarters Services, Directorate for Information Operations and Reports, 1215 Jefferson Davis Highway, Suite 1204, Arlington VA, 22202-4302. Respondents should be aware that notwithstanding any other provision of law, no person shall be subject to any penalty for failing to comply with a collection of information if it does not display a currently valid OMB control number.</p> <p>PLEASE DO NOT RETURN YOUR FORM TO THE ABOVE ADDRESS.</p>					
1. REPORT DATE (DD-MM-YYYY) 25-09-2017		2. REPORT TYPE Final Report		3. DATES COVERED (From - To) 28-Sep-2012 - 27-Sep-2015	
4. TITLE AND SUBTITLE Final Report: RF Energy Interaction With Electro-Optic Materials (Single investigator award proposed to address research topic area 6.4. Electromagnetics and RF Circuit Integration)			5a. CONTRACT NUMBER W911NF-12-1-0488		
			5b. GRANT NUMBER		
			5c. PROGRAM ELEMENT NUMBER 611102		
6. AUTHORS			5d. PROJECT NUMBER		
			5e. TASK NUMBER		
			5f. WORK UNIT NUMBER		
7. PERFORMING ORGANIZATION NAMES AND ADDRESSES Ohio State University 1960 Kenny Road  Columbus, OH 43210 -1016			8. PERFORMING ORGANIZATION REPORT NUMBER		
9. SPONSORING/MONITORING AGENCY NAME(S) AND ADDRESS (ES) U.S. Army Research Office P.O. Box 12211 Research Triangle Park, NC 27709-2211			10. SPONSOR/MONITOR'S ACRONYM(S) ARO		
			11. SPONSOR/MONITOR'S REPORT NUMBER(S) 62244-EL.13		
12. DISTRIBUTION AVAILABILITY STATEMENT Approved for public release; distribution is unlimited.					
13. SUPPLEMENTARY NOTES The views, opinions and/or findings contained in this report are those of the author(s) and should not be construed as an official Department of the Army position, policy or decision, unless so designated by other documentation.					
14. ABSTRACT					
15. SUBJECT TERMS					
16. SECURITY CLASSIFICATION OF:			17. LIMITATION OF ABSTRACT  UU	15. NUMBER OF PAGES	19a. NAME OF RESPONSIBLE PERSON Ronald Reano
a. REPORT UU	b. ABSTRACT UU	c. THIS PAGE UU			19b. TELEPHONE NUMBER 614-247-7204

**RPPR Final Report**  
as of 01-Nov-2017

Agency Code:

Proposal Number: 62244EL

**Agreement Number: W911NF-12-1-0488**

**INVESTIGATOR(S):**

**Name:** Ph.D. Ronald M. Reano

**Email:** reano.1@osu.edu

**Phone Number:** 6142477204

**Principal:** Y

Organization: **Ohio State University**

Address: 1960 Kenny Road, Columbus, OH 432101016

Country: USA

DUNS Number: 832127323

EIN: 316025986

**Report Date:** 27-Dec-2015

Date Received: 25-Sep-2017

**Final Report** for Period Beginning 28-Sep-2012 and Ending 27-Sep-2015

**Title:** RF Energy Interaction With Electro-Optic Materials (Single investigator award proposed to address research topic area 6.4. Electromagnetics and RF Circuit Integration)

**Begin Performance Period:** 28-Sep-2012

**End Performance Period:** 27-Sep-2015

**Report Term:** 0-Other

Submitted By: Ph.D. Ronald Reano

Email: reano.1@osu.edu

Phone: (614) 247-7204

**Distribution Statement:** 1-Approved for public release; distribution is unlimited.

**STEM Degrees:** 2

**STEM Participants:** 2

**Major Goals:** This project will capitalize the remarkable properties of hybrid ferroelectric and semiconductor materials. Under the framework of hybrid materials, unique opportunities are created to not only access some of the most surprising properties of materials but also to explore their interaction with RF energy to advance and develop a new class of radio frequency (RF)-optical devices and systems with unprecedented performance. The project brings together research concepts from RF engineering, optical physics, and material science allowing for both fundamental science and technological applications to be advanced in tandem. The goals of the research are threefold. First, the project focuses on the fundamental analysis and design of structures that couple RF and optical electromagnetic fields in a hybrid material system consisting of silicon and lithium niobate.

A hybrid material system consisting of both silicon and lithium niobate enables compact integrated optics on a silicon platform with electro-optic functionality provided by a true second order material susceptibility. We analyze the fundamental interaction of an RF electric field with an optical electric field in the hybrid material system.

Structures that effectively couple RF and optical electromagnetic fields are designed and analyzed using analytical and numerical techniques. Second, the project focuses on the fabrication of RF-optical coupling structures in the hybrid material system. Micrometer and nanometer scale fabrication techniques are created to realize structures that couple RF and optical electric fields in the silicon and lithium niobate hybrid material system. We develop methods to bond thin films of lithium niobate to patterned silicon. Metal films are used to concentrate the RF electric field in the vicinity of the optical electric field. Structures that effectively couple RF and optical electromagnetic fields are fabricated and evaluated under test and measurement. Third, the project focuses on RF-optical test and measurement demonstration vehicles. Test and measurement of fabricated structures will be conducted to experimentally quantify RF and optical performance. Measurement results will be compared with existing technologies and predictions from electromagnetic simulation.

**Accomplishments:** Please see the attached pdf document.

## RPPR Final Report as of 01-Nov-2017

**Training Opportunities:** One graduate student (Li Chen) and one undergraduate student (Jiahong Chen) received training related to RF and Optical technologies in a University Research Environment. The graduate student learned electromagnetic theory related to guided waves at both gigahertz frequencies and optical frequencies. The graduate student also was trained in advance nanoscale fabrication techniques for the development of coupled RF and optical structures. Both the graduate student and the undergraduate student were trained in conducting precision optical and RF measurements in the laboratory. The graduate student earned a PhD degree from this research project and the undergraduate student earned research experience during his senior year in undergraduate studies. Both students were trained to write documents for the purpose of archiving research results in technical journals.

**Results Dissemination:** Five journal papers and five conference papers have been published based on the research conducted for this project. The journal paper citations are:

1. L. Chen, J. Nagy, and R. M. Reano, "Patterned ion-sliced lithium niobate for hybrid photonic integration on silicon," *Optics Materials Express* 7, 2460-2467 (2016).
2. L. Chen, J. Chen, J. Nagy, and R. M. Reano, "Highly linear ring modulator from hybrid silicon and lithium niobate," *Optics Express* 23, 13255-13264 (2015).
3. L. Chen, M. Wood, and R. M. Reano, "Compensating thermal drift of hybrid silicon and lithium niobate ring resonances," *Optics Letters* 40, 1599-1602 (2015).
4. L. Chen, Q. Xu, M. Wood, and R. M. Reano, "Hybrid silicon and lithium niobate electro-optical ring modulator," *Optica* 1, 112-118 (2014).
5. Li Chen, Michael G. Wood, and Ronald M. Reano, "12.5 pm/V hybrid silicon and lithium niobate optical microring resonator with integrated electrodes," *Optics Express* 22, 27003-27010 (2013).

The conference paper citations are:

1. L. Chen, J. Nagy, and R. M. Reano, "(Invited) Patterning of Ion-Sliced Lithium Niobate for Hybrid Photonic Integration on Silicon," in *Conference on Lasers and Electro-Optics, 2016 OSA Technical Digest (online)* (Optical Society of America, 2016), paper SF1P.5.
2. L. Chen, J. Chen, J. Nagy, and R. M. Reano, "Hybrid Silicon and Lithium Niobate Racetrack Modulator with Large Spurious Free Dynamic Range," in *Conference on Lasers and Electro-Optics, 2015 OSA Technical Digest (online)* (Optical Society of America, 2015), paper STu2F.5.
3. L. Chen, M. G. Wood, and R. M. Reano, "Low Power Compensation of Thermal Drift in Hybrid Silicon and Lithium Niobate Ring Resonators," in *Frontiers in Optics, 2015 OSA Technical Digest (online)* (Optical Society of America, 2015), paper FTh3B.4.
4. L. Chen, Q. Xu, M. Wood, and R. M. Reano, "Gigahertz microring electro-optical modulator in hybrid silicon and lithium niobate," in *Frontiers in Optics, OSA Annual Meeting* (Optical Society of America, 2014), paper FTu1D.3.
5. L. Chen, M. Wood, and R. M. Reano, "Low Tuning Voltage Hybrid Silicon and Lithium Niobate Optical Microring Resonator with Integrated Electrodes," *Conference on Lasers and Electro-Optics (CLEO), San Jose, California* (2013).

**Honors and Awards:** Two papers from this research project received Outstanding Journal Article Awards at the Electroscience Laboratory, Department of Electrical and Computer Engineering, The Ohio State University.

1. L. Chen, J. Chen, J. Nagy, and R. M. Reano, "Highly linear ring modulator from hybrid silicon and lithium niobate," *Optics Express* 23, 13255-13264 (2015).
2. L. Chen, M. G. Wood, and R. M. Reano, "12.5 pm/V hybrid silicon and lithium niobate optical microring resonator with integrated electrodes," *Optics Express* 22, 27003-27010 (2013).

# RPPR Final Report

as of 01-Nov-2017

## Protocol Activity Status:

**Technology Transfer:** The research results generated one patent application filed with the United States Patent and Trademark Office through the Ohio State University. The patent application is titled "Patterned ion-sliced crystal for hybrid integrated photonics" by Ronald M. Reano and Li Chen. In the patent application is described a method of forming a deterministic thin film from a crystal substrate. The method can include implanting ions into a surface of the crystal substrate to form a thin film crystal layer, and bonding the crystal substrate and a handle substrate to form a bilayer bonding interface between the crystal substrate and the handle substrate. The method can also include exfoliating the thin film crystal layer from the crystal substrate, patterning the thin film crystal layer to define a deterministic thin film, etching one or more trenches in the thin film crystal layer, etching the bilayer bonding interface via the one or more trenches, and releasing the deterministic thin film from the handle substrate. The technology is enabling for future hybrid integrated photonic systems for communications, computing, and sensing.

## PARTICIPANTS:

**Participant Type:** PD/PI

**Participant:** Ronald M Reano

**Person Months Worked:** 12.00

**Funding Support:**

Project Contribution:

International Collaboration:

International Travel:

National Academy Member: N

Other Collaborators:

**Participant Type:** Graduate Student (research assistant)

**Participant:** Li Chen

**Person Months Worked:** 12.00

**Funding Support:**

Project Contribution:

International Collaboration:

International Travel:

National Academy Member: N

Other Collaborators:

**Participant Type:** Undergraduate Student

**Participant:** Jiahong Chen

**Person Months Worked:** 6.00

**Funding Support:**

Project Contribution:

International Collaboration:

International Travel:

National Academy Member: N

Other Collaborators:

## ARTICLES:



## RPPR Final Report as of 01-Nov-2017

**Publication Type:** Journal Article      Peer Reviewed: Y      **Publication Status:** 1-Published  
**Journal:** Optics Materials Express  
**Publication Identifier Type:** DOI      **Publication Identifier:** <https://doi.org/10.1364/OME.6.002460>  
**Volume:** 6      **Issue:** 7      **First Page #:** 2460  
**Date Submitted:** 9/22/17 12:00AM      **Date Published:** 7/1/16 4:00AM  
**Publication Location:**

**Article Title:** Patterned ion-sliced lithium niobate for hybrid photonic integration on silicon

**Authors:** Li Chen, Jonathan Nagy, Ronald M. Reano

**Keywords:** Integrated optics materials; Lithium Niobate; Integrated optics devices; Electro-optical devices; Resonators.

**Abstract:** A method to realize patterned ion-sliced lithium niobate is presented for hybrid photonic integration on silicon. The process involves indirect wafer bonding and dry etching to produce patterns with controllable size, shape, and orientation. The patterns are released by sacrificial wet etching and transferred to silicon waveguides using a pick-and-place process. To demonstrate the technique, a hybrid silicon and lithium niobate racetrack resonator with co-planar electrodes is presented with a measured tunability of 5.2 pm/V. The method enhances flexibility in design and control of fabrication yield for the realization of hybrid silicon and lithium niobate integrated optic devices.

**Distribution Statement:** 1-Approved for public release; distribution is unlimited.

**Acknowledged Federal Support:** Y

**Publication Type:** Journal Article      Peer Reviewed: Y      **Publication Status:** 1-Published  
**Journal:** Optics Express  
**Publication Identifier Type:** DOI      **Publication Identifier:** 10.1364/OE.23.013255  
**Volume:** 23      **Issue:** 10      **First Page #:** 13255  
**Date Submitted:** 9/22/17 12:00AM      **Date Published:** 5/1/15 4:00AM  
**Publication Location:**

**Article Title:** Highly linear ring modulator from hybrid silicon and lithium niobate

**Authors:** Li Chen, Jiahong Chen, Jonathan Nagy, Ronald M. Reano

**Keywords:** Integrated optics devices; Electro-optical devices; Modulators; Resonators; Lithium niobate; Radio frequency photonics.

**Abstract:** We present a highly linear ring modulator from the bonding of ion-sliced x-cut lithium niobate onto a silicon ring resonator. The third order intermodulation distortion spurious free dynamic range is measured to be 98.1 dB Hz<sup>2/3</sup> and 87.6 dB Hz<sup>2/3</sup> at 1 GHz and 10 GHz, respectively. The linearity is comparable to a reference lithium niobate Mach-Zehnder interferometer modulator operating at quadrature and over an order of magnitude greater than silicon ring modulators based on plasma dispersion effect. Compact modulators for analog optical links that exploit the second order susceptibility of lithium niobate on the silicon platform are envisioned.

**Distribution Statement:** 1-Approved for public release; distribution is unlimited.

**Acknowledged Federal Support:** Y

**Publication Type:** Journal Article      Peer Reviewed: Y      **Publication Status:** 1-Published  
**Journal:** Optics Letters  
**Publication Identifier Type:** DOI      **Publication Identifier:** 10.1364/OL.40.001599  
**Volume:** 40      **Issue:** 7      **First Page #:** 1599  
**Date Submitted:** 9/22/17 12:00AM      **Date Published:** 3/1/15 5:00AM  
**Publication Location:**

**Article Title:** Compensating thermal drift of hybrid silicon and lithium niobate ring resonances

**Authors:** Li Chen, Michael G. Wood, Ronald M. Reano

**Keywords:** Integrated optics devices; Sensors; Lithium niobate; Resonators; Optical interconnects.

**Abstract:** We present low-power compensation of thermal drift of resonance wavelengths in hybrid silicon and lithium niobate ring resonators based on the linear electro-optic effect. Fabricated devices demonstrate a resonance wavelength tunability of 12.5 pm/V and a tuning range of 1 nm. A capacitive geometry and low thermal sensitivity result in the compensation of 17°C of temperature variation using tuning powers at sub-nanowatt levels. The method establishes a route for stabilizing high-quality factor resonators in chip-scale integrated photonics subject to temperature variations

**Distribution Statement:** 1-Approved for public release; distribution is unlimited.

**Acknowledged Federal Support:** Y

**RPPR Final Report**  
as of 01-Nov-2017

**CONFERENCE PAPERS:**

**Publication Type:** Conference Paper or Presentation **Publication Status:** 1-Published  
**Conference Name:** CLEO: Science and Innovations  
Date Received: 22-Sep-2017 Conference Date: 09-Jun-2013 Date Published: 09-Jul-2013  
Conference Location: San Jose, California  
**Paper Title:** Low Tuning Voltage Hybrid Silicon and Lithium Niobate Optical Microring Resonator with Integrated Electrodes  
**Authors:** Li Chen, Michael Wood, Ronald M. Reano  
Acknowledged Federal Support: **Y**

**Publication Type:** Conference Paper or Presentation **Publication Status:** 1-Published  
**Conference Name:** Frontiers in Optics  
Date Received: 22-Sep-2017 Conference Date: 19-Oct-2014 Date Published: 19-Oct-2014  
Conference Location: Tucson, Arizona  
**Paper Title:** Gigahertz Microring Electro-Optical Modulator in Hybrid Silicon and Lithium Niobate  
**Authors:** Li Chen, Qiang Xu, Michael Wood, Ronald M. Reano  
Acknowledged Federal Support: **Y**

**Publication Type:** Conference Paper or Presentation **Publication Status:** 1-Published  
**Conference Name:** Frontiers in Optics  
Date Received: 22-Sep-2017 Conference Date: 18-Oct-2015 Date Published: 18-Oct-2014  
Conference Location: San Jose, California  
**Paper Title:** Low Power Compensation of Thermal Drift in Hybrid Silicon and Lithium Niobate Ring Resonators  
**Authors:** Li Chen, Michael G. Wood, Ronald M. Reano  
Acknowledged Federal Support: **Y**

**Publication Type:** Conference Paper or Presentation **Publication Status:** 1-Published  
**Conference Name:** CLEO: Science and Innovations  
Date Received: 22-Sep-2017 Conference Date: 10-May-2015 Date Published: 10-May-2015  
Conference Location: San Jose, California  
**Paper Title:** Hybrid Silicon and Lithium Niobate Racetrack Modulator with Large Spurious Free Dynamic Range  
**Authors:** Li Chen, Jiahong Chen, Jonathan Nagy, Ronald M. Reano  
Acknowledged Federal Support: **Y**

**Publication Type:** Conference Paper or Presentation **Publication Status:** 1-Published  
**Conference Name:** CLEO: Science and Innovations  
Date Received: 22-Sep-2017 Conference Date: 05-Jun-2016 Date Published: 05-Jun-2016  
Conference Location: San Jose, California  
**Paper Title:** Patterning of Ion-Sliced Lithium Niobate for Hybrid Photonic Integration on Silicon  
**Authors:** Li Chen, Jonathan Nagy, Ronald M. Reano  
Acknowledged Federal Support: **Y**

**DISSERTATIONS:**

**RPPR Final Report**  
as of 01-Nov-2017

**Publication Type:** Thesis or Dissertation

**Institution:** The Ohio State University

**Date Received:** 22-Sep-2017

**Completion Date:** 4/21/15 8:27PM

**Title:** Hybrid Silicon and Lithium Niobate Integrated Photonics

**Authors:** Li Chen

**Acknowledged Federal Support:** Y

**PATENTS:**

**Intellectual Property Type:** Patent

**Date Received:** 22-Sep-2017

**Patent Title:** Patterned ion-sliced crystal for hybrid integrated photonics

**Patent Abstract:** An example method of forming a deterministic thin film from a crystal substrate is described

**Patent Number:** 15/612,087

**Patent Country:** USA

**Application Date:** 02-Jun-2017

**Application Status:** 1

**Date Issued:**

## SECTION: ACCOMPLISHED UNDER GOALS WITH FIGURES AND REFERENCES

### A. DESIGN.

We have designed structures on the micro-scale to efficiently couple RF and optical energy in the hybrid silicon and lithium niobate material system. A schematic of a tunable hybrid silicon and lithium niobate ( $\text{LiNbO}_3$ ) microring resonator is shown in Fig. 1(a). The resonator consists of a silicon rib waveguide microring and a  $\text{LiNbO}_3$  thin film bonded to the silicon resonator as a portion of the top cladding via BCB. The silicon rib waveguides are 500 nm wide with a 70 nm slab thickness and 180 nm rib height. A bottom metal electrode is formed around and exterior to the microring on the silicon slab to provide an electric path to the silicon core. A top metal electrode is aligned to the microring on top of the  $\text{LiNbO}_3$  thin film and a  $\text{SiO}_2$  buffer layer that is deposited by plasma enhanced chemical vapor deposition (PECVD). Figure 1(b) shows a schematic of the cross-section of the device structure.

The  $\text{LiNbO}_3$  thin film and the PECVD  $\text{SiO}_2$  buffer layer serve as the top cladding. On the cross-section of the microring waveguide, a portion of the optical guided-mode is within the  $\text{LiNbO}_3$  thin film. Figure 2(a) shows the fraction of the optical mode power within the  $\text{LiNbO}_3$  thin film as a function of the thickness of the  $\text{LiNbO}_3$  thin film for the transverse electric (TE) and transverse magnetic (TM) modes, at 1550 nm optical wavelength, calculated using the semi-vector beam propagation method (BPM). In the simulation, the PECVD  $\text{SiO}_2$  layer below the aluminum electrode is set to be 1  $\mu\text{m}$  thick. The refractive indices of silicon,  $\text{SiO}_2$ ,  $\text{LiNbO}_3$  and BCB are set to 3.48, 1.44, 2.14 and 1.54, respectively, in the simulation. The maximum fraction of the optical mode power in the  $\text{LiNbO}_3$  approaches 42% for the TM mode and 11% for the TE mode as the  $\text{LiNbO}_3$  thickness approaches 1  $\mu\text{m}$ . The larger optical mode field overlap with the  $\text{LiNbO}_3$  for the TM mode is desirable for greater tuning efficiency. Moreover, the TM mode accesses the  $r_{33}$  electro-optic coefficient in  $\text{LiNbO}_3$ , whereas the TE mode accesses the  $r_{13}$  electro-optic coefficient ( $r_{33} = 31 \text{ pm V}^{-1}$ ,  $r_{13} = 8 \text{ pm V}^{-1}$  in bulk  $\text{LiNbO}_3$ ) [1,2]. Therefore, the device is designed for the TM mode. Furthermore, the fraction of the optical mode power in the  $\text{LiNbO}_3$  for the TM mode is marginally improved for  $\text{LiNbO}_3$  thicknesses greater than 600 nm. The thickness of the  $\text{LiNbO}_3$  is therefore chosen to be 800 nm.

The use of the silicon microring as a transparent conductor minimizes the dielectric layer thickness required to isolate the optical mode from the electrodes [3]. As a result, the voltage induced electric field inside the  $\text{LiNbO}_3$  cladding layer is enhanced thereby enabling a larger change in the refractive index of the  $\text{LiNbO}_3$  via the linear electro-optic effect. The PECVD  $\text{SiO}_2$  cladding layer thickness significantly influences the electric field intensity in the  $\text{LiNbO}_3$  ( $\epsilon_z = 29.1$ ) [1] thin film since the permittivity of  $\text{LiNbO}_3$  is much higher than that of PECVD  $\text{SiO}_2$  (relative permittivity  $\epsilon_r = 4.2$ ) [4]. The red curve in Fig. 2(b) shows the vertical (perpendicular to the surface of the substrate) electric field intensity ( $E_z$ ) of the applied DC field in the  $\text{LiNbO}_3$  thin film as a function of the PECVD  $\text{SiO}_2$  thickness simulated using the finite element method (FEM) electro-static solver. The electric field distribution within  $\text{LiNbO}_3$  is not uniform due to the rib topology of the silicon waveguide. Therefore, the electric fields are evaluated at the center of the  $\text{LiNbO}_3$  thin film directly above the center of the silicon waveguide. For an 800 nm thick  $\text{LiNbO}_3$  thin film and an applied voltage of 1 V between the top electrode and the silicon core,  $E_z$  in the  $\text{LiNbO}_3$  thin film decreases from 1.15 V/ $\mu\text{m}$  to 0.45 V/ $\mu\text{m}$  as the PECVD  $\text{SiO}_2$  layer increases from 0 nm to 300 nm.

A thinner PECVD  $\text{SiO}_2$  layer is desirable for achieving higher electric field in  $\text{LiNbO}_3$ . Conversely, reducing the PECVD  $\text{SiO}_2$  thickness leads to optical loss from the optical mode interacting with the top aluminum electrode. The blue curve in Fig. 2(b) shows the TM mode optical loss caused by the aluminum electrode at 1550 nm wavelength, as a function of the PECVD  $\text{SiO}_2$  thickness, calculated by BPM. In the simulation, the imaginary part of the refractive index of aluminum is set to 16 [5]. The thickness of the PECVD  $\text{SiO}_2$  layer is chosen to be 125 nm. Relatively large electric fields in the  $\text{LiNbO}_3$  and metal-induced optical loss less than 0.2 dB/cm are expected.

Figure 3(b) shows the cross-section electric field distribution of the design for the fundamental TM mode at 1550 nm optical wavelength calculated using BPM. Material boundaries are indicated by the white dashed lines and the material regions are indicated in the insets. The BCB thickness is 0 nm in the simulation. The effective index is calculated to be 2.3.

A second design that focuses on high frequency performance and the utilization of the transverse electric (TE) mode is shown in Fig. 4. The cross-section is through the center of the ring resonator. The device consists of a 15  $\mu\text{m}$  radius silicon rib waveguide ring and a one micrometer thick z-cut ion-sliced  $\text{LiNbO}_3$  thin film bonded via BCB [6]. The rib waveguides are 500 nm wide with a 45 nm slab thickness and 205 nm rib height. The silicon slab is patterned so that it exists only around and exterior to the ring. The silicon core and surrounding silicon slab layer are doped to function as a transparent conductor with reduced series resistance [7]. A voltage applied between the top electrode and the bottom electrode produces an electric field confined between the top electrode and the silicon waveguide core.

The 1550 nm wavelength TE optical mode distribution is shown in Fig. 5 calculated by BPM. The effective index of the optical mode is 2.66. Also shown is the voltage induced electric field (yellow vectors) from a DC voltage applied between the top electrode and the silicon transparent conductor, using material permittivities in finite element method calculations [8,9,10].

The optical mode and the electric field vectors overlap in the  $\text{LiNbO}_3$ . The fraction of the optical mode power in the  $\text{LiNbO}_3$  is 11%. The TE mode accesses the  $r_{13}$  electro-optic coefficient in  $\text{LiNbO}_3$  ( $r_{13} = 8 \text{ pm V}^{-1}$  in bulk  $\text{LiNbO}_3$ ) [9] and takes advantage of the nearly vertical voltage induced electric field in the  $\text{LiNbO}_3$ .

The device speed is limited by the RC time constant and the photon lifetime in the ring resonator [11]. The electrical resistance originates primarily from the silicon transparent conductor and the contact resistance. To reduce the resistance, the silicon waveguide is blanket implanted with P-type dopants at a light dose, followed by a P-type heavy dose on the slab. The heavily-doped region is 300 nm away from the silicon core to avoid excessive optical loss.

The two previous designs utilized z-cut lithium niobate. In the third design, x-cut lithium niobate is utilized in order to incorporate co-planar electrodes. A schematic of the hybrid silicon and  $\text{LiNbO}_3$  structure is shown in Fig. 6. The device consists of a silicon strip waveguide ring resonator and a 1  $\mu\text{m}$  thick x-cut ion-sliced  $\text{LiNbO}_3$  thin film bonded via BCB [12]. The ring radius is 10  $\mu\text{m}$  on the curves and is 50  $\mu\text{m}$  in length on the straight sections. The cross-section of the silicon strip waveguide is 550 nm  $\times$  170 nm and the coupling gap between the bus waveguide and the ring is 180 nm. The z crystal axis of the  $\text{LiNbO}_3$  is oriented perpendicular to the propagation direction of the straight sections of the ring.

Metal electrodes are placed on top of the  $\text{LiNbO}_3$  thin film with a 1  $\mu\text{m}$  lateral electrode gap aligned to the center of the silicon core. The electrodes are interdigitated so that the directions of the applied electric fields in the two straight waveguide sections are the same. As a result, the phase change accumulates constructively as light propagates along the racetrack ring. The configuration allows the device to access the  $r_{33}$  electro-optic coefficient along the straight waveguide sections for the transverse-electric (TE) optical waveguide mode. A large ratio of straight section length to curved section length around the ring is desirable because the modulation efficiency is weaker along the arcs.

Figure 7 shows the TE mode optical distribution in a straight waveguide section at 1550 nm calculated via the beam propagation method. The mode effective index is 2.45 and the fraction of the optical mode power in the  $\text{LiNbO}_3$  is 25%. Also shown is the electric field (yellow vectors) from a DC voltage applied between the top metal electrodes. The high optical confinement allows the top side metal electrodes to be placed close to each other and over the waveguide without inducing large optical absorption loss, enabling a large electric field for a given applied voltage. The capacitance per unit length of the electrode is calculated to be 0.2 pF/m based on finite element method simulations. A device capacitance of 30 fF and resistance of 30  $\Omega$  yields an RC limited bandwidth of 66 GHz in a 50  $\Omega$  system. As a result, the device speed is limited by the photon lifetime of the resonator.

## B. FABRICATION

In this phase of the research, a method was developed to produce patterned thin films of ion-sliced  $\text{LiNbO}_3$  for hybrid photonic integration on silicon. Thin films of  $\text{LiNbO}_3$  with deterministic shape and crystal orientation are obtained with edge lengths in the range of hundreds of microns to several millimeters. The patterned  $\text{LiNbO}_3$  thin films are transferred and bonded to silicon waveguides using a pick-and-place process [13]. Patterning allows the crystal axes of  $\text{LiNbO}_3$  to be identified for electrode orientation.

The process to obtain patterned ion-sliced  $\text{LiNbO}_3$  is illustrated in Fig. 8 using x-cut  $\text{LiNbO}_3$  wafers as an example. A 3-inch x-cut  $\text{LiNbO}_3$  wafer of 500  $\mu\text{m}$  thickness is diced into rectangular samples with edge lengths ranging from 0.5 cm to 3 cm. The x-cut  $\text{LiNbO}_3$  sample is implanted with  $\text{He}^+$  ions with an implantation energy of 380 keV and a fluence of  $3.5 \times 10^{16}$  ions  $\text{cm}^{-2}$ , as shown in Fig. 8(a). During ion implantation, Ag paste is applied between the  $\text{LiNbO}_3$  sample and the sample holder to enhance thermal dissipation. The beam current density is maintained at 0.25  $\mu\text{A cm}^{-2}$  and the total implantation time is seven hours. The temperature of the wafer holder increases gradually during the implantation but remains below 100  $^\circ\text{C}$ .

After ion implantation, the  $\text{LiNbO}_3$  sample is cleaned using RCA1 solution and clad with 1  $\mu\text{m}$  of plasma enhanced chemical vapor deposition (PECVD)  $\text{SiO}_2$ . The PECVD  $\text{SiO}_2$  layer will serve as a sacrificial layer to release the ion-sliced  $\text{LiNbO}_3$  later in the process. A second x-cut  $\text{LiNbO}_3$  handle wafer is cleaned with RCA1 and coated with adhesion promoter (Dow Chemical AP3000) and BCB (Dow Chemical CYCLOTENE 3022-35), as shown in Fig. 8(b). The implanted wafer is coated with adhesion promoter and bonded to the  $\text{LiNbO}_3$  handle wafer via the BCB film. The crystal z axes of the wafers, which are along the edges of the wafers, are aligned to each other under a microscope. The bonded wafer pair is heated gradually to 300  $^\circ\text{C}$  in an oven in an  $\text{N}_2$  ambient. First, the oven temperature is ramped to 200  $^\circ\text{C}$  linearly from room temperature over a period of one hour. The sample is then held at 200  $^\circ\text{C}$  for one hour. The temperature is then increased by 10  $^\circ\text{C}$  every hour until a final temperature of 250  $^\circ\text{C}$  is reached, where the sample is held at 250  $^\circ\text{C}$  for one hour [14]. During the ramping process, the BCB is fully cured, strengthening the bond. Concurrently, micro-bubbles are formed in the ion-damaged layer, leading to exfoliation of the implanted layer [14]. Finally the wafer pair is heated to 300  $^\circ\text{C}$  over a period of 2 hours and held for one hour before being gradually cooled down to room temperature over a period of 5 hours. As a result, 1.1  $\mu\text{m}$  thick ion-sliced  $\text{LiNbO}_3$  is exfoliated from the implanted wafer and transferred to the handle wafer, as shown in Fig. 8(d).

Figure 9(a) shows the transferred  $\text{LiNbO}_3$  thin film on the handle wafer. The cross sectional area of the thin film is approximately 0.85 cm by 1.2 cm. A thin film stack of ion-sliced  $\text{LiNbO}_3$ , PECVD  $\text{SiO}_2$ , and BCB is formed on the surface of the handle wafer, as shown in Fig. 9(b). The root mean square (rms) surface roughness of the transferred thin film is 39 nm, measured with atomic force microscopy. The surface roughness can be reduced to sub-nanometer level by chemical mechanical polishing [15].

The areal shape of the ion-sliced  $\text{LiNbO}_3$  is defined by a Cr mask patterned by electron beam lithography (EBL) and plasma etching. A 320 nm thick Cr layer is first deposited on the surface. The sample is then deposited with 300 nm PECVD  $\text{SiO}_2$  and coated with 660 nm polymethyl methacrylate (PMMA) resist. The PMMA resist is patterned by EBL and serves as a mask to etch the PECVD  $\text{SiO}_2$  layer by inductively coupled plasma reactive ion etching (ICP-RIE) using  $\text{CHF}_3$  chemistry. Here, the patterns are in rectangular shapes with edge sizes in the range of hundreds of micrometers. The spacing between each rectangular pattern is 5  $\mu\text{m}$ . After PMMA resist removal, the Cr mask is formed using the PECVD  $\text{SiO}_2$  mask by ICP-RIE using  $\text{Cl}_2$  and  $\text{O}_2$  chemistry, as shown in Fig. 10(a). The ion-sliced  $\text{LiNbO}_3$  is then etched through to the BCB using the Cr mask by ICP-RIE using Ar and  $\text{CHF}_3$  chemistry. The etching rate of  $\text{LiNbO}_3$  is 10 nm/min and the etching selectivity to the Cr mask is 5:1. Five micron wide trenches are formed between each ion-sliced  $\text{LiNbO}_3$  rectangular pattern.

After dry etching, the Cr mask is removed with CR-7S chromium etchant, as shown in Fig. 10(b). The sample is then etched in 5% hydrofluoric (HF) acid to undercut the PECVD SiO<sub>2</sub> layer underneath the ion-sliced LiNbO<sub>3</sub> from the etched trenches between patterns, as shown in Fig. 10(c). The horizontal undercut etching rate is approximately 5  $\mu\text{m}/\text{min}$ . Figure 11(a) shows the undercut after etching for 4 minutes. Before the ion-sliced LiNbO<sub>3</sub> is fully released by etching, the LiNbO<sub>3</sub> sample is flipped to an unpolished silicon substrate and the etching is resumed with both substrates in the etchant. After etching for 12 min, the ion-sliced LiNbO<sub>3</sub> patterns break away from the SiO<sub>2</sub> pillar. The samples are then rinsed in DI water and dried on a hotplate at 80  $^{\circ}\text{C}$ , completing the transfer of the LiNbO<sub>3</sub> films to the unpolished silicon substrate, as illustrated in Fig. 10(d). Figure 11(b) shows patterned ion-sliced LiNbO<sub>3</sub> on the silicon surface with edge lengths of 100  $\mu\text{m} \times 150 \mu\text{m}$  and 100  $\mu\text{m} \times 450 \mu\text{m}$ . The maximum pattern size achieved is 100  $\mu\text{m} \times 2 \text{ mm}$ . The z-axis of the crystal is along the short edges of the patterns. One corner of the patterns is etched so that the crystal axes can be identified. Rapid thermal annealing (RTA) is then performed at 1000  $^{\circ}\text{C}$  for 30 s to repair the crystal lattice and restore the electro-optical properties of the ion-sliced LiNbO<sub>3</sub> [15].

Device fabrication proceeds as illustrated in Fig. 12. The silicon waveguides are patterned from hydrogen silsesquioxane (HSQ) resist using EBL and ICP-RIE [16]. The sample is coated with BCB and then baked in a N<sub>2</sub> ambient to planarize the surface. Next, the sample is heated to partially cure the BCB. Partial curing helps prevent BCB reflow that may occur after bonding [17]. The BCB is then etched back using ICP-RIE with O<sub>2</sub> and CF<sub>4</sub> chemistry. LiNbO<sub>3</sub> samples prepared on a silicon substrate are transferred to the silicon racetrack using a glass micro-vacuum tip on a probe station. The micro-vacuum tip has a hose diameter of 25  $\mu\text{m}$  and is connected to a vacuum source by plastic tubing. The z-axis of the LiNbO<sub>3</sub> along the short edge of the pattern is aligned to the bus waveguide. The sample is baked to cure the BCB and complete the bonding.

After bonding, the sample is capped with PECVD SiO<sub>2</sub>. An access hole is formed by removing the SiO<sub>2</sub> film over the racetrack resonator using ICP-RIE. Metal electrodes are patterned in the access hole with a two-step lithography process to accurately control the narrow electrode gap. The signal electrode is first formed. Then, the ground electrode is aligned to the signal electrode in the second lithography step. An electrode gap is formed with an alignment error smaller than 50 nm. Finally, cantilever couplers are patterned for fiber-to-chip optical coupling [18]. Figure 13 shows top-view optical micrographs of a fabricated device after bonding and electrode patterning.

### C. DEMONSTRATION

Demonstration vehicles in the form of gigahertz speed RF electro-optical modulators were developed. Optical transmission measurements were performed to characterize the electrical tuning of optical resonances. Optical light from a tunable infrared continuous-wave laser source was coupled through the input and output fiber-to-chip cantilever couplers of the modulator. DC voltage is applied to the top electrode of the modulator while the bottom electrode is grounded. Figure 14 shows the measured optical mode spectrum as a function of the applied DC voltage. The resonance wavelength redshifts with increasingly positive voltage. The total optical insertion loss for this device is 4.3 dB. The insertion loss is from 3 dB of fiber-to-waveguide coupling loss and 1.3 dB of waveguide transmission loss. The decrease of the optical transmission minimum with voltage is attributed to Fabry-Pérot fringes present due to fiber-to-chip coupling. The resonance shift is 66 pm for a change in DC bias from -10 V to 10 V, indicating 3.3 pm/V tuning, which is equivalent to a V <sub>$\pi$</sub> L of 9.1 V-cm. The measured quality factor is 14,000, the full-width half-maximum is 13.7 GHz, and the group index is 4.0. At 1551.856 nm, the optical transmission intensity varies by 5.2 dB with a -5 V to 5 V voltage swing, as indicated by the dashed arrow in Fig. 14.

The RF scattering parameter, S<sub>11</sub>, is measured with a 20 GHz vector network analyzer (VNA) operating in a 50  $\Omega$  system. Figure 15(a) shows the measured S<sub>11</sub> magnitude and phase data. The magnitude of S<sub>11</sub> drops sharply to -2 dB from 40 MHz to 2 GHz, and then gradually rolls off to -4.5 dB at 20 GHz. An RC circuit model extracted from

the measured  $S_{11}$  is shown in Fig. 15(b) [19]. Parameter  $R_C$  denotes the resistance of the metal electrodes. Parameter  $C_P$  represents the parasitic capacitance between the metal electrodes through the top dielectric materials and the air. Parameters  $C_J$  and  $R_S$  model the electrical path through the silicon transparent electrode and the  $\text{LiNbO}_3$  layer. Parameters  $C_{OX}$  and  $R_{Si}$  model the electrical path through the buried oxide and the silicon substrate. The value of  $C_J$  is in good agreement with finite element method simulations. The relatively high value of  $R_S$  indicates a lower than expected doping concentration in the waveguide and a higher than expected contact resistance [20]. The relatively large  $C_P$  value is mainly attributed to the parasitic capacitance of the electric pads. The sharp drop at the lower frequency band is attributed to the RF coupling through the substrate.

The small-signal electrical-to-optical modulation response is shown in Fig. 16. The modulated optical signal is detected with a photodetector with a 3 dB bandwidth of 12 GHz. Also shown in Fig. 16 is the frequency response of the voltage across  $C_J$  in the circuit model shown in Fig. 15(b). The measured 3 dB optical response bandwidth of the modulator is approximately 5 GHz. While the general trend of the optical responses match the circuit model, the optical response contains additional dips and peaks across the entire frequency band.

The dips and peaks on the optical modulation response are a result of acousto-optic resonances [21,22,23]. The electric fields between the electrodes excite acoustic waves in the 1  $\mu\text{m}$  thick  $\text{LiNbO}_3$  producing resonances in the gigahertz frequency range. Multiple resonance peaks apparent in the  $S_{11}$  measurements at 1.7 GHz and corresponding harmonics indicate the conversion of the electrical energy to acoustic energy at the acoustic resonances. Consequently, refractive index changes occur in the  $\text{LiNbO}_3$  through the elasto-optic effect. The acoustic resonances can be suppressed by roughening the surface of the piezoelectric material to increase the scattering loss of the acoustic wave [24,25]. The surface roughness can be produced by dry or wet etching. Sufficiently thick  $\text{LiNbO}_3$  avoids optical mode interaction with the rough surface.

A schematic for high-speed digital modulation characterization is shown in Fig. 17 [19]. A pulse pattern generator (PPG) outputs a  $2^{31}-1$  pseudo-random-bit-stream data stream (PRBS31) with a voltage swing from -1 V to 1V. The peak-to-peak amplitude of the signal is amplified to 5 V (-2.5V to 2.5 V) with a modulator driver amplifier. The output light from the modulator is passed through a fiber amplifier and an optical passband filter with 0.5 nm bandwidth to amplify the signal and suppress the amplified spontaneous emission noise. The amplified optical signal is attenuated and connected to a 30 GHz optical module on a digital communication analyzer (DCA) synchronized to the clock of the PPG for generating optical eye diagrams. The optical bias wavelength is tuned to maximize the extinction ratio (ER).

The left column of Fig. 18 shows measured optical eye diagrams at 1 Gb/s, 4.5 Gb/s, 5 Gb/s, and 9 Gb/s, with extinction ratios of 4.7 dB, 4.5 dB, 4 dB and 3 dB, respectively. The right column of Fig. 18 shows simulated eye diagrams at the corresponding bit rates with ideal PRBS driving signals. The extinction ratio and shape of the simulated optical eyes agree well with the measurement results. In particular, the amplitude ringing for the 1 Gb/s eye and the partial eye closing on the left part of the 5 Gb/s eye closely match the simulation.

The total energy consumption of the modulator is estimated to be 4.4 pJ/bit at 9 Gb/s with a 10 V swing. The energy per bit encompasses 0.4 pJ/bit from  $C_J$ , 1.8 pJ/bit from  $C_P$ , and 2.2 pJ/bit from  $C_{OX}$ . The energy consumption on  $C_J$  is only 9% of the total energy consumption. The majority of the energy consumption is attributed to charging and discharging of the large area electrical pads for test and measurement. Energy consumption can be reduced by optimizing device capacitances. Steady state DC power consumption for tuning of optical resonance frequencies is ideally zero in the capacitive device.



## FIGURES

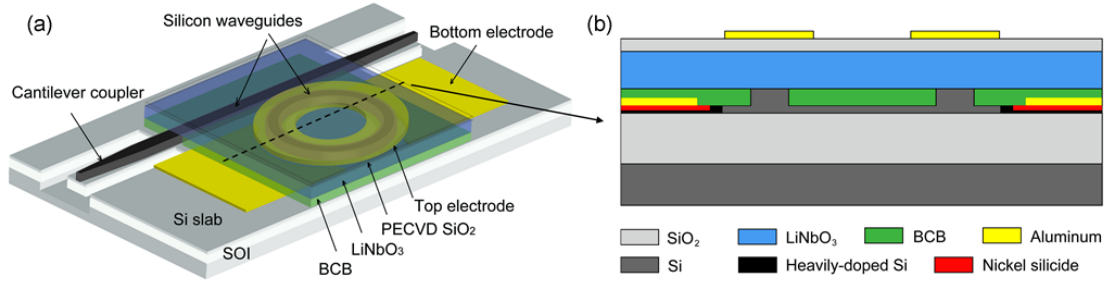


Fig. 1. (a) Schematic of a tunable hybrid silicon and LiNbO<sub>3</sub> microring resonator with integrated electrodes. (b) Schematic of the cross-section of the device structure along the dashed line shown in (a). The design is intended for transverse magnetic (TM) optical modes.

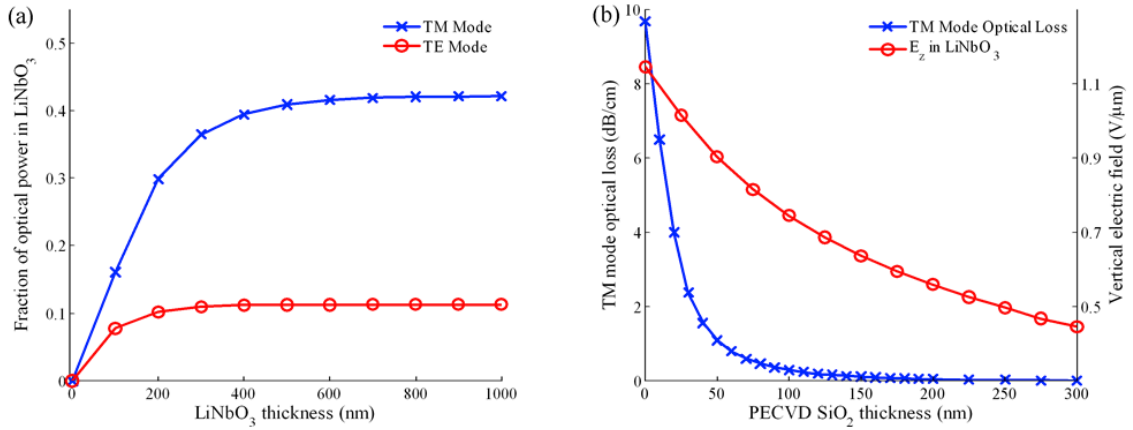


Fig. 2. (a) Beam Propagation Method (BPM) calculations of the optical mode power in LiNbO<sub>3</sub> versus the thickness of LiNbO<sub>3</sub> for the transverse magnetic (TM) mode and the transverse electric (TE) mode in the hybrid Si/LiNbO<sub>3</sub> structure. (b) Calculations of the optical loss (blue) induced by the top aluminum electrode and the voltage induced vertical electric field in LiNbO<sub>3</sub> (red) versus the PECVD silicon dioxide thickness. The LiNbO<sub>3</sub> thin film thickness is set to be 800 nm and the applied voltage is 1 V.

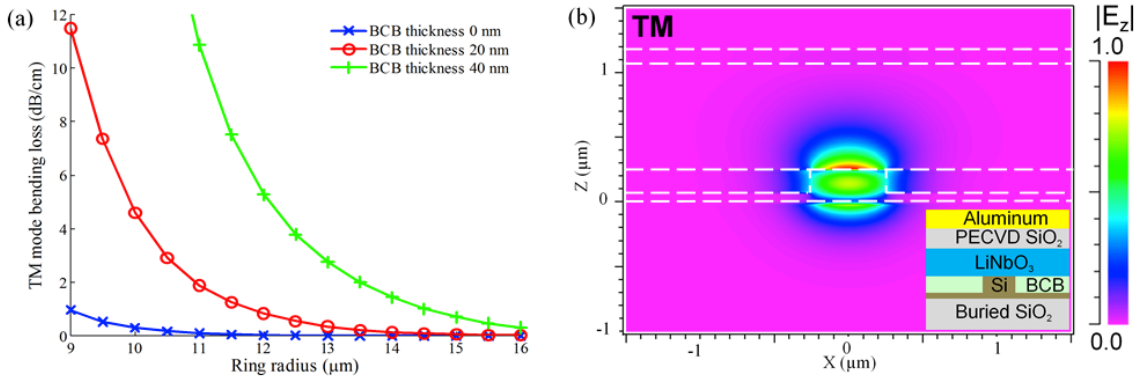


Fig. 3. (a) Calculated TM mode optical bending loss versus the ring radius for BCB thickness of 0 nm, 20 nm, and 40 nm between the top of the silicon core and the bottom of the LiNbO<sub>3</sub> thin film. (b) Calculated optical electric field distribution of the hybrid silicon and LiNbO<sub>3</sub> structure for the fundamental TM mode at 1550 nm wavelength ( $E_z$  component).

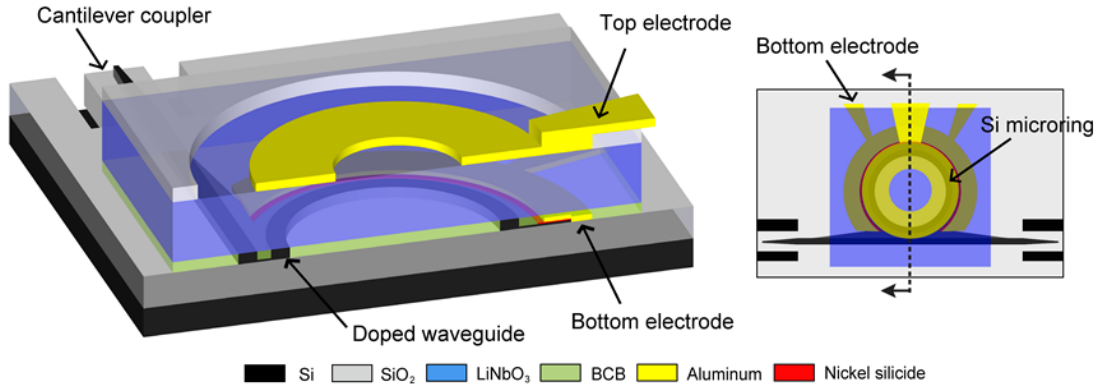


Fig. 4. Schematic of hybrid silicon and lithium niobate ring resonator designed for high electrical frequency operation and in the transverse electric (TE) optical mode.

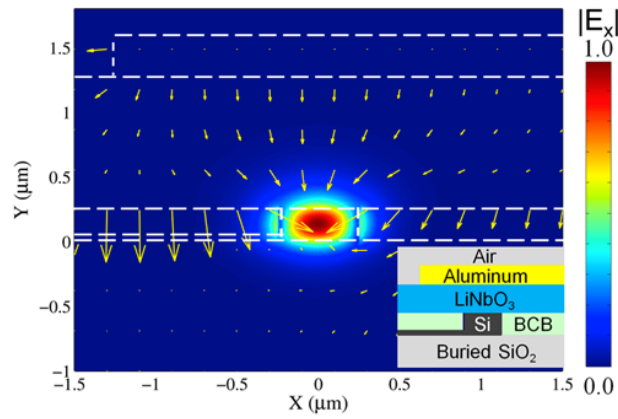


Fig. 5. Calculated optical TE mode distribution at 1550 nm wavelength ( $E_x$  component) and DC voltage induced electric field vectors.

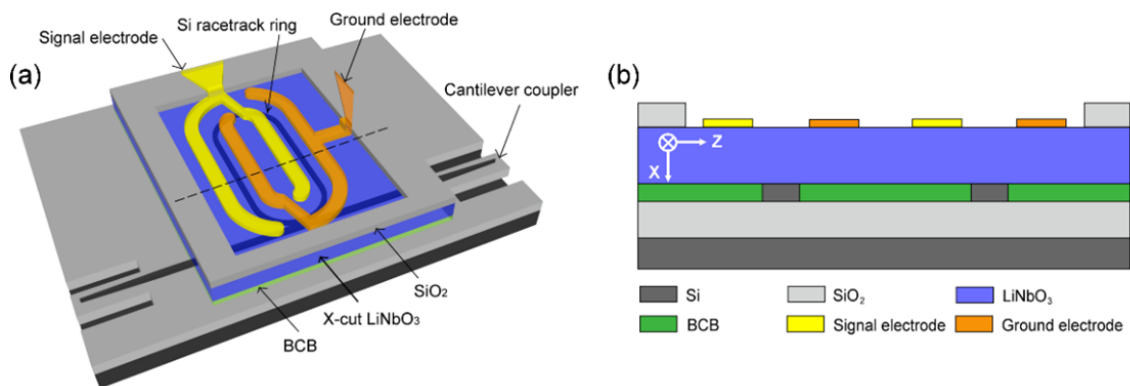


Fig. 6. (a) Schematic of hybrid Si/LiNbO<sub>3</sub> ring modulator. For clarity, the PECVD SiO<sub>2</sub> top-cladding layer and electrical contact pads are not shown. (b) Schematic of cross-section of device along dashed line in (a).

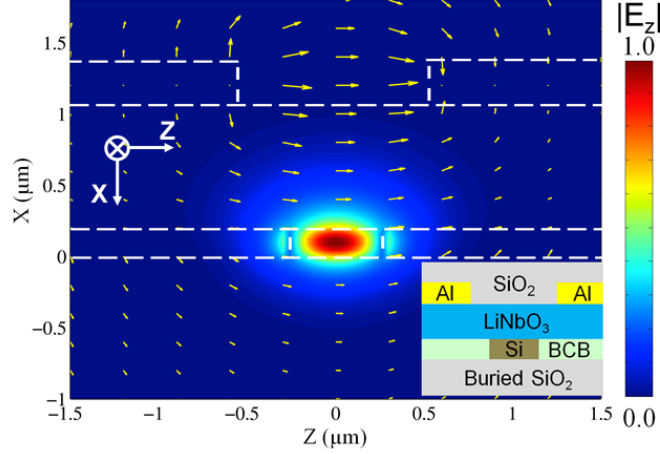


Fig. 7 Calculated optical TE mode distribution at 1550 nm wavelength and electric field vectors from applied DC voltage.

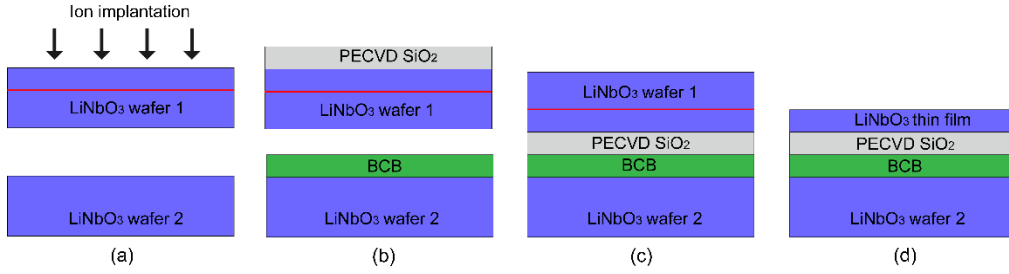


Fig. 8. Ion-sliced LiNbO<sub>3</sub> exfoliation: (a) He<sup>+</sup> ion implantation on wafer 1, (b) PECVD SiO<sub>2</sub> deposition on wafer 1 and BCB spin-coating on wafer 2, (c) wafer bonding and annealing, (d) exfoliation of ion-sliced LiNbO<sub>3</sub>.

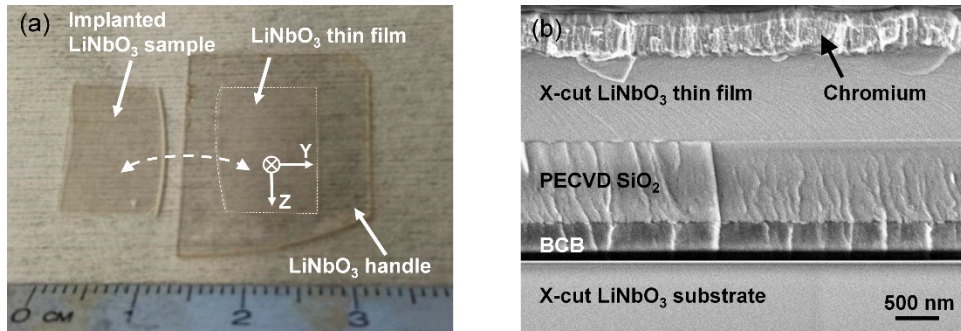


Fig. 9. (a) X-cut ion-sliced LiNbO<sub>3</sub> bonded to a LiNbO<sub>3</sub> handle substrate. The wafers are diced into rectangular samples for identification and alignment of the crystal z-axes. (b) Scanning electron micrograph (SEM) of the cross-section of the thin film stack. The dark line in the BCB layer is due to charging during the scanning electron microscopy.

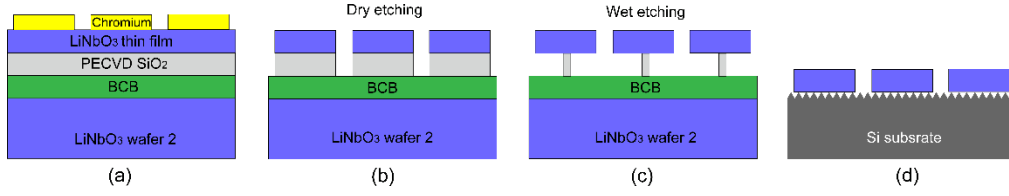


Fig. 10. Patterned ion-sliced LiNbO<sub>3</sub> fabrication flow: (a) patterning Cr mask, (b) dry etching of LiNbO<sub>3</sub>, (c) wet etching of PECVD SiO<sub>2</sub>, (d) Transferring LiNbO<sub>3</sub> to an unpolished silicon substrate.

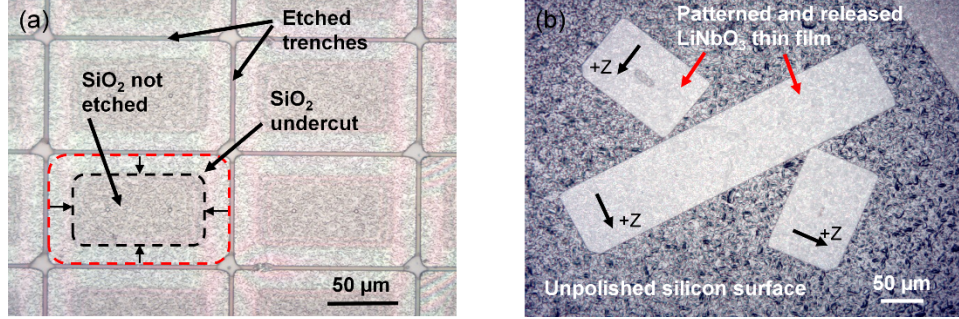


Fig. 11. (a) HF acid etching of the patterned x-cut ion-sliced LiNbO<sub>3</sub>; (b) Released ion-sliced LiNbO<sub>3</sub> transferred to the unpolished surface of a silicon substrate.

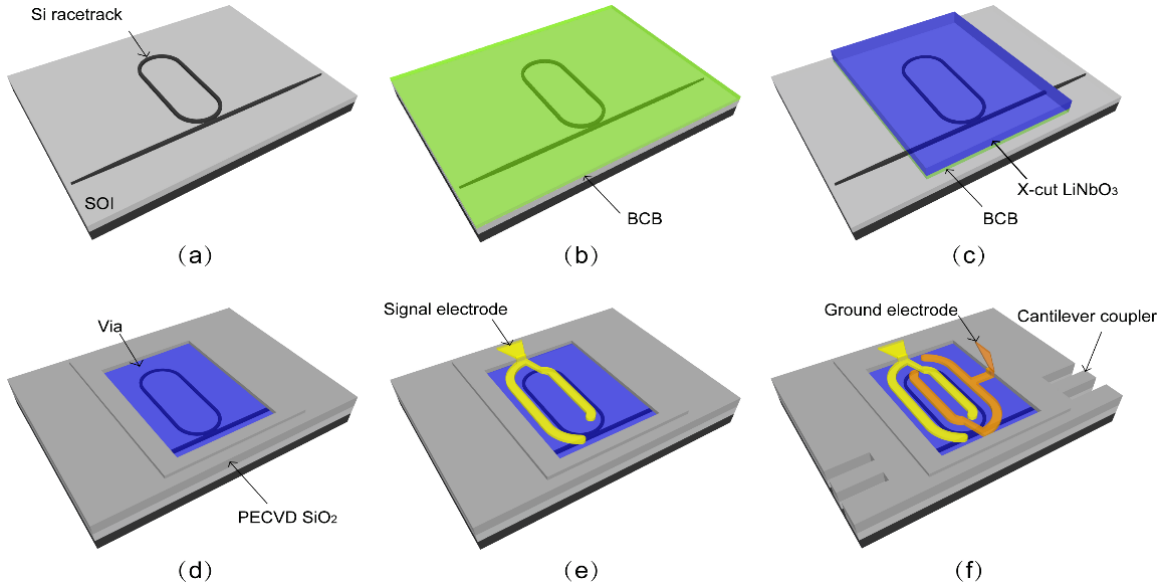


Fig. 12. Fabrication process of Si/LiNbO<sub>3</sub> racetrack resonator: (a) Silicon strip patterned on silicon-on-insulator wafer using EBL and plasma etching; (b) spin-coat, partial curing, and etch back of BCB; (c) bonding of LiNbO<sub>3</sub> and plasma etch of BCB; (d) deposition of PECVD SiO<sub>2</sub> and removal of SiO<sub>2</sub> above the resonator; (e) patterning of signal electrode; (f) patterning of ground electrode and cantilever couplers.

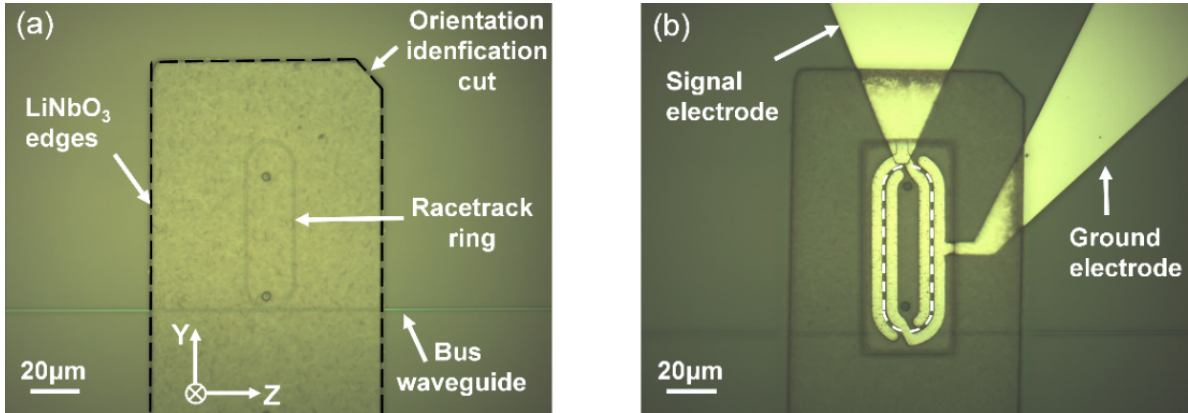


Fig. 13. Top-view optical micrograph of fabricated Si/LiNbO<sub>3</sub> racetrack resonator. (a) Image of device after bonding of the LiNbO<sub>3</sub>; (b) Image of device after patterning of the electrodes.

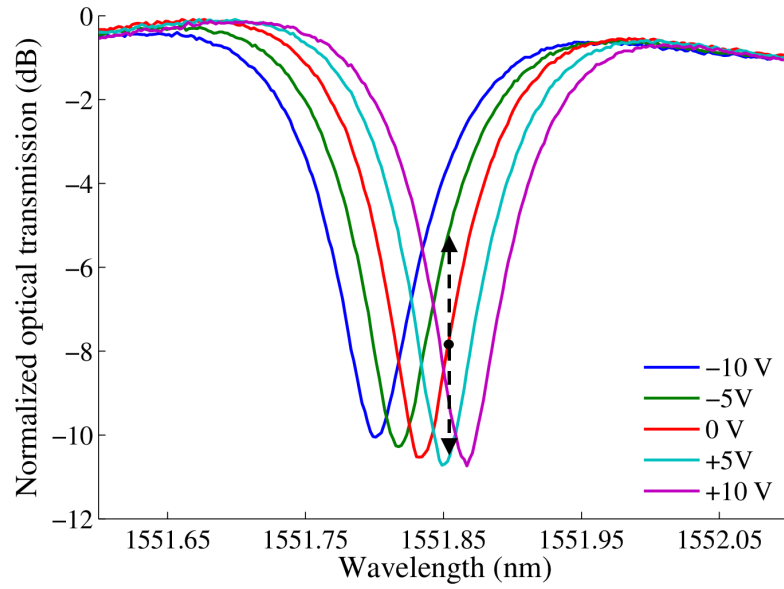


Fig. 14. Measured optical transmission of a single resonance as a function of applied voltage.

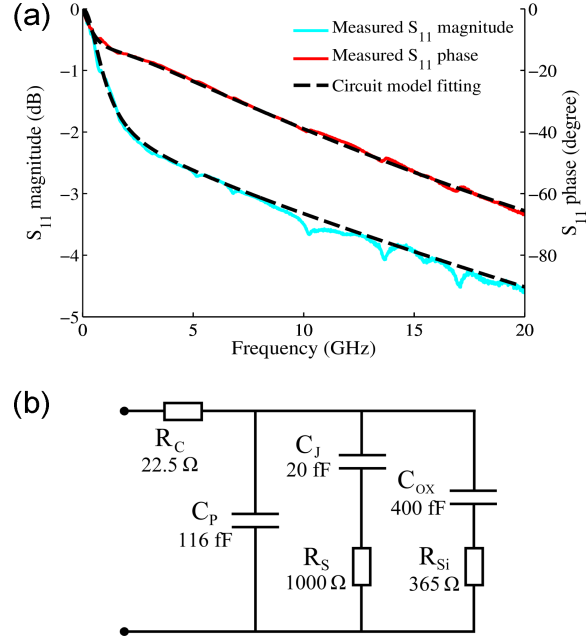


Fig. 15. (a) RF  $S_{11}$  scattering parameter; (b) RC circuit model of the modulator.

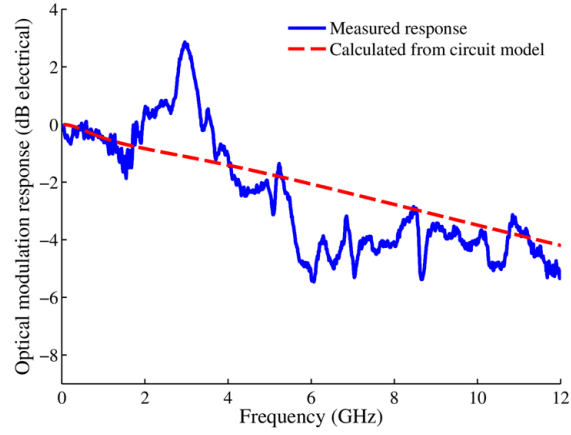


Fig. 16. Electrical-to-optical modulation response.

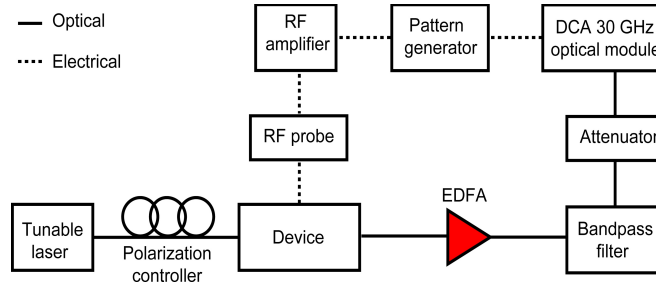


Fig. 17. Measurement setup for digital characterization



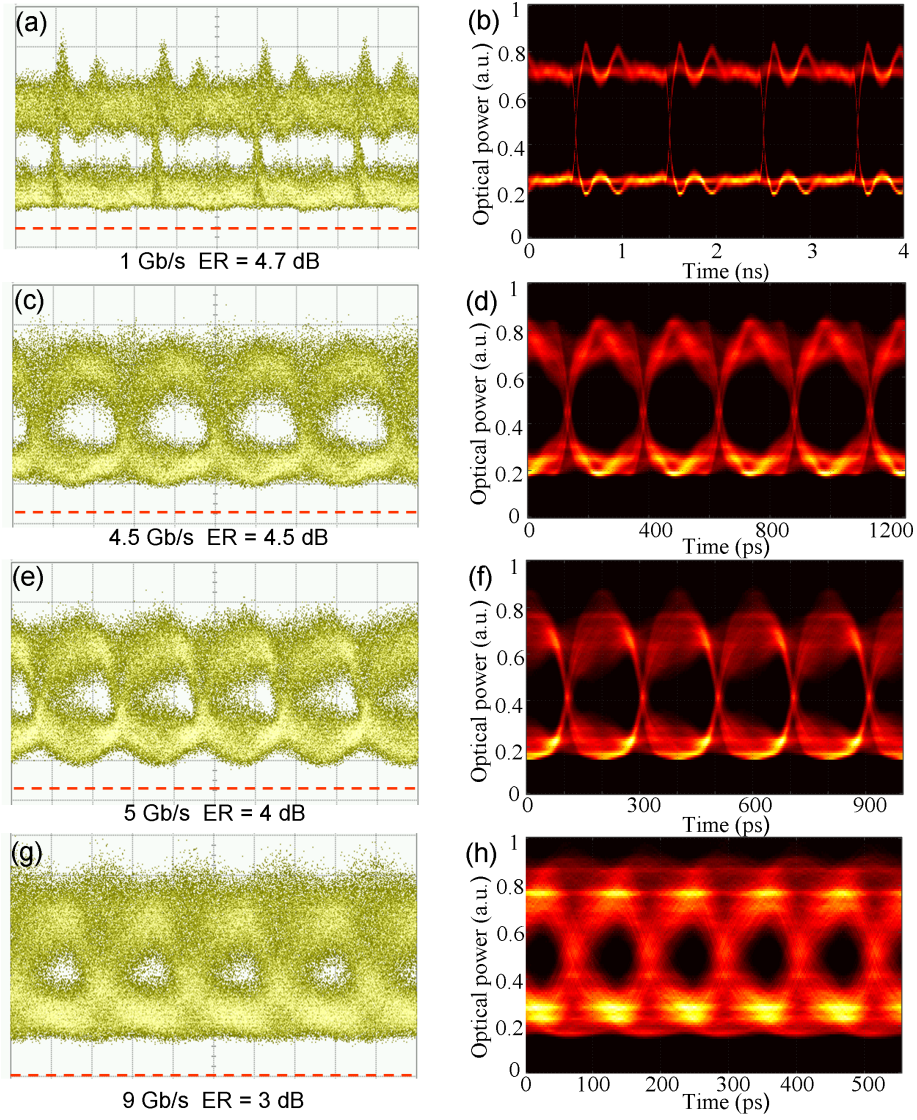


Fig. 18. Measured (left column) and simulated (right column) optical eye: (a) and (b) 1 Gb/s, (c) and (d) 4.5 Gb/s, (e) and (f) 5 Gb/s, (g) and (h), 9 Gb/s. The red dashed line in the measurement indicates the reference level for zero optical input. The vertical scale is 500  $\mu\text{W}$  per division.

## REFERENCES

1. K. K. Wong, *Properties of Lithium Niobate* (INSPEC, 2002).
2. M. Jazbinšek and M. Zgonik, "Material tensor parameters of  $\text{LiNbO}_3$  relevant for electro- and elasto-optics," *Appl. Phys. B* **74**, 407-414 (2002).
3. M. Hochberg, T. Baehr-Jones, G. Wang, J. Huang, P. Sullivan, L. Dalton, and A. Scherer, "Towards a millivolt optical modulator with nano-slot waveguides," *Opt. Express* **15**(13), 8401–8410 (2007).
4. M. F. Ceiler, Jr., P. A. Kohl, and S. A. Bidstrup, "Plasma-enhanced chemical vapor deposition of silicon dioxide deposited at low temperatures," *J. Electrochem. Soc.*, **142**(6), 2067-2071 (1995).
5. E. D. Palik, ed., *Handbook of Optical Constants of Solids*, vol. 1 (Academic Press, 1998).
6. L. Chen and R. M. Reano, "Compact electric field sensors based on indirect bonding of lithium niobate to silicon microrings," *Opt. Express* **20**, 4032-4038 (2012).
7. L. Chen, M. G. Wood, and R. M. Reano, "12.5 pm/V hybrid silicon and lithium niobate optical microring resonator with integrated electrodes," *Opt. Express* **21**, 27003-27010 (2013).
8. K. K. Wong, *Properties of Lithium Niobate* (INSPEC, 2002).
9. M. E. Mills, P. Townsend, D. Castillo, S. Martin, and A. Achen, "Benzocyclobutene (DVS-BCB) polymer as an interlayer dielectric (ILD) material," *Microelectron. Eng.* **33**, 327-334 (1997).
10. S. M. Sze, and K. K. Ng, *Physics of Semiconductor Devices* (Wiley, 1981).
11. G. T. Reed, G. Mashanovich, F. Y. Gardes, and D. J. Thomson, "Silicon optical modulators," *Nat. Photonics* **4**, 518–526 (2010).
12. Li Chen, Qiang Xu, Michael G. Wood, and Ronald M. Reano, "Hybrid silicon and lithium niobate electro-optical ring modulator," *Optica* **1**, 112-118 (2014).
13. M. Koechlin, F. Sulser, Z. Sitar, G. Poberaj, and P. Günter, "Free-standing lithium niobate microring resonators for hybrid integrated optics," *IEEE Photon. Technol. Lett.* **22**(4), 251–253 (2010).
14. L. Chen and R. M. Reano, "Compact electric field sensors based on indirect bonding of lithium niobate to silicon microrings," *Opt. Express* **20**(4), 4032-4038 (2012).
15. P. Rabiei and P. Gunter, "Optical and electro-optical properties of submicrometer lithium niobate slab waveguides prepared by crystal ion slicing and wafer bonding," *Appl. Phys. Lett.* **85**(20), 4603–4605 (2004).
16. M. Wood, L. Chen, J. R. Burr, and R. M. Reano, "Optimization of electron beam patterned hydrogen silsesquioxane mask edge roughness for low-loss silicon waveguides," *J. Nanophoton.* **8**(1), 083098 (2014).
17. F. Niklaus, R. Kumar, J.J. McMahon, J. Yu, J. -Q. Lu, T. S. Cale, and R. J. Gutmann, "Adhesive wafer bonding using partially cured benzocyclobutene for three-dimensional integration," *J. Electrochem. Soc.* **153**(4), G291–G295 (2006).
18. P. Sun and R. M. Reano, "Cantilever couplers for intra-chip coupling to silicon photonic integrated circuits," *Opt. Express* **17**(6), 4565-4574 (2009).
19. G. Li, X. Zheng, J. Yao, H. Thacker, I. Shubin, Y. Luo, K. Raj, J. E. Cunningham, and A. V. Krishnamoorthy, "25Gb/s 1V-driving CMOS ring modulator with integrated thermal tuning," *Opt. Express* **19**, 20435–20443 (2011).
20. R. Ding, T. Baehr-Jones, Y. Liu, R. Bojko, J. Witzens, S. Huang, J. Luo, S. Benight, P. Sullivan, J.-M. Fedeli, M. Fournier, L. Dalton, A. Jen, and M. Hochberg, "Demonstration of a low  $V_\pi L$  modulator with GHz bandwidth based on electro-optic polymer-clad silicon slot waveguides," *Opt. Express* **18**, 15618–15623 (2010).
21. J. L. Nightingale, R. A. Becker, R. C. Willis, and J. S. Vrhel, "Characterization of frequency dispersion in Ti-diffused lithium niobate optical devices," *Appl. Phys. Lett.* **51**, 716-718 (1987).
22. R. L. Jungerman and C. A. Flory, "Low-frequency acoustic anomalies in lithium niobate Mach-Zehnder interferometers," *Appl. Phys. Lett.* **53**, 1477–1479 (1988).
23. W. K. Burns, M. M. Howerton, R. P. Moeller, R. Krähenbühl, R. W. McElhanon, and A. S. Greenblatt, "Low drive voltage, broad-band  $\text{LiNbO}_3$  modulators with and without etched ridges," *J. Lightwave Technol.*, **17**, 2551–2555, (1999).



24. A. Vorobiev, J. Berge, S. Gevorgian, M. Löffler, and E. Olsson, “Effect of interface roughness on acoustic loss in tunable thin film bulk acoustic wave resonators,” *J. Appl. Phys.* **110**, 024116 (2011).
25. M. Yoshida, S. Okamoto, T. Omiya, K. Kasai, and M. Nakazawa, “256 QAM digital coherent optical transmission using Raman amplifiers,” *IEICE Trans. Commun.*, **E94-B**, 417–424, (2011).